Version of Record: https://www.sciencedirect.com/science/article/pii/S0168900220307476
Manuscript_1fb1840386c616d425e5acb2bd9ed37c

Computation of beam based quantities with 3D final focus quadrupoles field in circular hadronic accelerators.

T. Pugnat, B. Dalena

CEA, Irfu, DACM, Université Paris-Saclay, F-91191, Gif-sur-Yvette, France

A. Simona, L. Bonaventura

MOX, Politecnico di Milano, Milano, Italy

Abstract

The computation of analytic and numerical beam based quantities are derived for full 3D representation of the quadrupoles magnetic field, which can be computed by finite element code or measured. The impact of this more accurate description of the non homogeneity of the field is estimated on beam based observables and non linear correctors strengths, and compared with the less accurate models in the case of HL-LHC.

Keywords: Non-linear beam dynamics, Optics corrections, Chaotic motion

1. Introduction

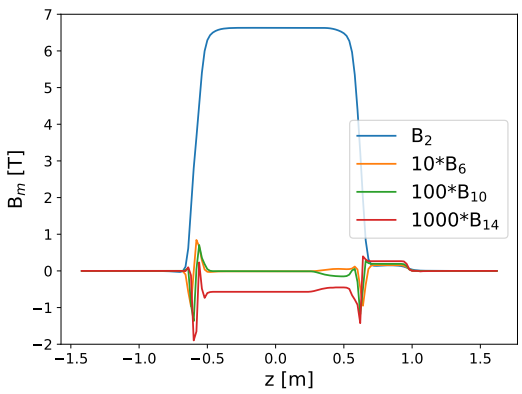

Figure 1: Normal longitudinal harmonics sampled at $\Delta z = 2$mm for the prototype of HL-LHC Inner Triplet quadrupole. Courtesy of E. Todesco and S. Izquierdo Bermudez.

Email addresses: thomas.pugnat@cea.fr (T. Pugnat), barbara.dalena@cea.fr (B. Dalena)

This paper presents the computation of beam based quantities (such as amplitude detuning and dynamic aperture) based on a 3D representation of the non homogeneity's of the quadrupole field, studying, in particular, the final focus quadrupoles of the high luminosity upgrade of LHC (HL-LHC [1]).

In general, allowed non linearities are stronger in the extremities than in the body of a magnet, as can be seen in Fig. 1, where the longitudinal profile of the harmonics from a short prototype of the large aperture (150 mm) final focus quadrupoles of HL-LHC project is shown. The presence of connectors on one side of the magnet has also been considered since they break the longitudinal symmetry of the field. In this paper, the orientation of the magnet follow the power scheme for HL-LHC shown in Fig. 2.

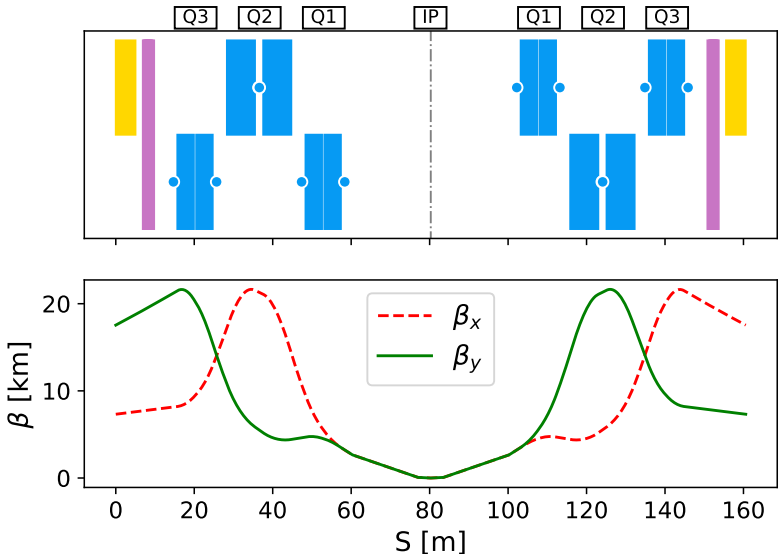

Figure 2: Single aperture elements in the HL-LHC insertion regions. The three (splitted) quadrupoles composing each inner triplet (Q1, Q2 and Q3) are in blue, blue dots represent the position of the quadrupoles connectors, the first separation dipole is in yellow and the non-linear correctors are in purple (top panel). The horizontal and vertical β functions are shown in the bottom panel.

The possibility to study the impact of magnet fringe fields on non-linear beam dynamics dates back to around the 90's [2, 3]. More recently, analytical functions have been used to fit magnetic field data, computed with finite element codes or measured, with application to different projects [4, 5]. Generalized Gradients based methods are also able to include magnetic data, measured or computed, in the non-linear transfer maps [6, 7]. Its application to a photon source [8] have shown agreement of tracking simulations using magnetic field maps with tracking using machine optics model. Here, we fully link the Generalised Gradient technique to beam based observables, to study the impact of the 3 dimensional distribution of the field on the ring performance. We consider the case of HL LHC inner triplet where the gradient of the betatronic (β) function

in a single quadrupole is not so small and the β function is very big. Therefore, beam based quantities like Amplitude Detuning and Dynamic Aperture, are dominated by the errors in these elements.

Combining the variation of this high β function in the same quadrupole and a non-uniform longitudinal distribution of the harmonic alongside the magnet can have a non-negligible weight on the model prediction and explain eventual discrepancy with beam based observables. In particular, this study quantifies the level of detail in the description of the field that has significant effect on commonly used beam based quantities, such as amplitude detuning, dynamic aperture and non linear correctors evaluations. An analytical calculations of the impact of the extremities of the inner triplet magnets of HL-LHC on detuning with amplitude, using first order Hamiltonian perturbation theory can be found in [9]. In this paper, we derived it for the first time in terms of generalized gradients of the magnetic field, including also the dodecapole harmonics, and extend it to the numerical estimates of the same quantities studied in the previous paper and of the dynamic aperture, comparing it to more simplified models for the non-linear transfer maps.

Section 2 describes the analytical calculation for the variation of the phase-space transverse angular velocity with the amplitude of the particle (Amplitude Detuning) in terms of Generalized Gradients of the quadrupole. This beam dynamic quantity is widely used to define the performance and the non-linear correction in circular accelerators [10]. Beam based measurements of amplitude detuning are essential for the LHC commissioning [11].

Section 3 introduces the symplectic and efficient (mandatory for application to large hadron storage rings) non-linear transfer maps based on Generalized Gradients and compares it to the approximated models: the classical one, in which the non-linearities of the field are integrated along the magnet and uniformly distributed, and a first approximation of the longitudinal distribution of the high order harmonics, which splits the quadrupole into three parts (i.e. the body and the two extremities). The proposed 3D non-linear transfer map, called Lie2 since is derived using Lie Algebra techniques, consists of numerical integration of the two extremities using smaller steps. It has the advantage (with respect to the approximate models) to be able to take into account the derivatives of the field gradients, that are also sources of non-linearites.

Section 4 compares the analytical estimates of Amplitude Detuning (AD) with the tracking simulations using the three different transfer maps, corresponding to the models described in the previous section. This beam-based observable refers to the variation of the transverse Phase-Space angular frequency (i.e. the tune) with respect to the amplitude of the particle and it is the most direct measurement of beam non-linearities. The impact of the model on the correctors strength expected to correct this AD, is also quantified and compared to present strength specifications. Those correctors are used to correct locally non-linearities (i.e. reduce the beam Resonance Driving Terms (RDTs), Ref. [12]).

Section 5 repeats the comparison of the models on another beam dynamic quantity that is the Dynamic Aperture. It defines the region of stable mo-

tion of the particles against magnet non-linearities and is often used to define tolerances on magnets conception in the design phase of circular accelerators. Unlike Amplitude Detuning, there is no analytic calculation of Dynamic Aperture including field errors and corrections. Its computation relies on tracking simulations therefore an accurate, symplectic and efficient non linear transfer map is necessary for large hadrons storage rings, as the LHC.

2. Expression of the Amplitude Detuning with generalized gradients

Following Ref. [13], the Amplitude and Cross Detuning as a function of the normalized amplitude $2J_u$ ($u \in \{x, y\}$) is given by:

$$\Delta Q_u = \frac{1}{2\pi} \oint \frac{\partial \langle H_p \rangle}{\partial J_u} \mathrm{d}i \tag{1}$$

with $\langle H_p \rangle$ the perturbative part of the Hamiltonian, describing the non-homogeneity's of the field, and i the position along the ring. In this paper, the kinematic and second order terms will be neglected. Following Ref. [13], the equations for the Direct and Cross Amplitude Detuning for the harmonics b_4 and b_6 are:

$$\begin{aligned}
\Delta Q_x &= \frac{q}{2\pi p_0 c} \sum_i \Big[\frac{3}{8} \left(\beta_x^2 \bar{b}_4\right)_i (2J_x) + \frac{5}{16} \left(\beta_x^3 \bar{b}_6\right)_i (2J_x)^2 \\
&\quad - \frac{3}{4} \left(\beta_x \beta_y \bar{b}_4\right)_i (2J_y) + \frac{15}{16} \left(\beta_x \beta_y^2 \bar{b}_6\right)_i (2J_y)^2 \\
&\quad - \frac{15}{8} \left(\beta_x^2 \beta_y \bar{b}_6\right)_i (2J_x 2J_y) \Big] \qquad (2) \\
\Delta Q_y &= \frac{q}{2\pi p_0 c} \sum_i \Big[\frac{3}{8} \left(\beta_y^2 \bar{b}_4\right)_i (2J_y) - \frac{5}{16} \left(\beta_y^3 \bar{b}_6\right)_i (2J_y)^2 \\
&\quad - \frac{3}{4} \left(\beta_x \beta_y \bar{b}_4\right)_i (2J_x) - \frac{15}{16} \left(\beta_x^2 \beta_x \bar{b}_6\right)_i (2J_x)^2 \\
&\quad + \frac{15}{8} \left(\beta_x \beta_y^2 \bar{b}_6\right)_i (2J_x 2J_y) \Big] \qquad (3)
\end{aligned}$$

where the $\overline{b_n}$ indicates that the relative high order field harmonics are averaged for the positions i belonging to the same element and are kept constant over the length of the magnet. They can be computed with finite element codes or measured with rotating coils. Using expression (14) of the Generalized Gradient and $H_p = -a_z - a_x p_x - a_y p_y$ being the perturbative Hamiltonian with the vector potential defined in Eq. 15, the previous equations can be extended to consider the gradient derivatives and different values for the field harmonics along the same element:

$$\begin{aligned}
\Delta Q_x &= \frac{q}{2\pi p_0 c} \sum_i \Big[\frac{3}{8} \left(4\beta_x^2 C_{4,s}^{[0]} + 2\beta_x \alpha_x C_{2,s}^{[1]} - \frac{2}{3} \beta_x^2 C_{2,s}^{[2]}\right)_i 2J_x \\
&\quad - \frac{3}{4} \left(4\beta_x \beta_y C_{4,s}^{[0]} - \frac{1}{3}(\beta_x \alpha_y - \beta_y \alpha_x) C_{2,s}^{[1]}\right)_i 2J_y \\
&\quad + \frac{5}{16} \left(6\beta_x^3 C_{6,s}^{[0]} + \frac{3}{2} \beta_x^2 \alpha_x C_{4,s}^{[1]} - \frac{9}{20} \beta_x^3 C_{4,s}^{[2]}\right)_i (2J_x)^2 \qquad (4) \\
&\quad + \frac{15}{16} \left(6\beta_x \beta_y^2 C_{6,ts}^{[0]} + \frac{1}{5} \beta_y \left(\frac{\beta_y \alpha_x}{2} - 3\beta_x \alpha_y\right) C_{4,s}^{[1]} + \frac{3}{20} \beta_x \beta_y^2 C_{4,s}^{[2]}\right)_i (2J_y)^2 \\
&\quad - \frac{15}{8} \left(6\beta_x^2 \beta_y C_{6,s}^{[0]} - \frac{1}{5} \beta_x \left(\frac{\beta_x \alpha_y}{2} - 3\beta_y \alpha_x\right) C_{4,s}^{[1]} - \frac{3}{20} \beta_x^2 \beta_y C_{4,s}^{[2]}\right)_i 2J_x 2J_y \Big]
\end{aligned}$$

$$
\begin{aligned}
\Delta Q_y \quad = \quad & \frac{q}{2\pi p_0 c}\sum_i \Bigg[\frac{3}{8}\left(4\beta_y^2 C_{4,s}^{[0]} - 2\beta_y\alpha_y C_{2,s}^{[1]} + \frac{2}{3}\beta_y^2 C_{2,s}^{[2]}\right)_i 2J_y \\
& -\frac{3}{4}\left(4\beta_x\beta_y C_{4,s}^{[0]} - \frac{1}{3}(\beta_x\alpha_y - \beta_y\alpha_x)C_{2,s}^{[1]}\right)_i 2J_x \\
& -\frac{5}{16}\left(6\beta_y^3 C_{6,s}^{[0]} - \frac{3}{2}\beta_y^2\alpha_y C_{4,s}^{[1]} + \frac{9}{20}\beta_y^3 C_{4,s}^{[2]}\right)_i (2J_y)^2 \\
& -\frac{15}{16}\left(6\beta_x^2\beta_y C_{6,s}^{[0]} - \frac{1}{5}\beta_x\left(\frac{\beta_x\alpha_y}{2} - 3\beta_y\alpha_x\right)C_{4,s}^{[1]} - \frac{3}{20}\beta_x^2\beta_y C_{4,s}^{[2]}\right)_i (2J_x)^2 \\
& +\frac{15}{8}\left(6\beta_x\beta_y^2 C_{6,s}^{[0]} + \frac{1}{5}\beta_y\left(\frac{\beta_y\alpha_x}{2} - 3\beta_x\alpha_y\right)C_{4,s}^{[1]} + \frac{3}{20}\beta_x\beta_y^2 C_{4,s}^{[2]}\right)_i 2J_x 2J_y\Bigg]
\end{aligned}
\tag{5}
$$

From these equations, it appears clearly that the non-linearities act on amplitude detuning as weighted sum of the multipolar strengths with the Twiss parameters as weight powers. In regions where those weights can vary inside one magnet and/or have big values, not taking into consideration the longitudinal distribution of the non-linear harmonics can bias the prediction for the detuning with Amplitude. The same holds for the RDTs with also additional dependence on the phases advances.

3. The Lie2 non-linear transfer map

In order to describe the motion of the particles in a magnetic system, the transfer map of the system is required and in the case of multi-turn simulations in the large hadron collider, this map needs also to be symplectic. Using Lie Algebra formalism, a non-linear and symplectic transfer map takes the following expression:

$$M(\Delta\sigma) = \exp(-L : K :) \tag{6}$$

where L and K are respectively the length and the Hamiltonian of the system. In order to have the explicit dependence on z in the Hamiltonian, we consider the 8 dimensions Hamiltonian reported in appendix A. Since the expression of the Hamiltonian contains the terms of the type $(p_{x,y} - a_{x,y})^2$, the system is not exactly solvable, so we use a transfer map approximated to the second order (that we call Lie2):

$$
\begin{aligned}
M(\Delta\sigma) \quad = \quad & \exp(\frac{-\Delta\sigma}{2} : K1 :)\exp(-\frac{\Delta\sigma}{2} : K2 :)\exp(-\frac{\Delta\sigma}{2} : K3 :)\exp(-\Delta\sigma : K4 :) \\
& \exp(-\frac{\Delta\sigma}{2} : K3 :)\exp(-\frac{\Delta\sigma}{2}\sigma : K2 :)\exp(-\frac{\Delta\sigma}{2} : K1 :) + O(\Delta\sigma^3) \\
= \quad & M2 + O(\Delta\sigma^3)
\end{aligned}
\tag{7}
$$

where $K1 = pz - \delta$, $K2 = a_z$, $K3 = \frac{(p_x - a_x)^2}{2(1+\delta)}$, $K4 = \frac{(p_y - a_y)^2}{2(1+\delta)}$, $: K : f =< K, f >$ is the Lie operator defined by the Poisson brackets [14], and we have used the generating function given in [15] to simplify the terms K3 and K4. To optimize the computational speed this Lie2 transfer map is applied only at the two extremities of the quadrupoles magnet (which are the same of the magnet prototype). The central part of the quadrupole (called body) is treated in the hard hedge approximation since all the harmonics are expected to be constant

(Ref. [16, 17, 18]). As specified in Ref. [19], this model also allows to consider the derivatives of the gradient in the simulation, another source of non-linearities which is not included in the hard edge approximation of the kicks. In the following, ND0 represents the case without derivatives of the field gradients, and ND6 the case with the derivatives up to the 6^{th}. The impact of the number of derivatives (ND, derivative orders) is discussed in appendix B, while details of the numerical implementation of the Lie2 transfer map and its integration in the SixTrack tracking code are reported in appendix A.

This new map is compared with classical kicks models using hard hedge approximation applied on one optics configuration of the HL-LHC project. The goal is to verify if the harmonics longitudinal distribution have a measurable impact on beam-based observable. A schematic view of these three models is shown in Fig. 3. As a matter of convention, we use the notation of the magnetic length L and the normalized strength b_n where n is the order of the harmonic (2 for quadrupole, ...), etc, and indices T, CS, NC and B represent respectively the whole magnet, the connector and non-connector side, and the body.

In the Hard Edge model, called HE, the harmonic longitudinal distribution and their derivatives are neglected. The normalized integrated strength $b_{n,T}L_T$ is equally distributed on 16 multipolar kicks for each quadrupole.

In the model called HE+Heads, the normalized integrated strengths in the extremity (Head) of the quadrupole ($b_{n,CS}L_{CS}$ and $b_{n,NC}L_{NC}$) are estimated, respectively as $L_{NC/CS} = \int_{NC/CS} \frac{B_2}{B_{2,max}} \mathrm{d}z$ and $\overline{b_{n,NC/CS}} = \int_{NC/CS} \frac{B_n}{B_{2,max} L_{NC/CS}} \mathrm{d}z$, using the two halves of the longitudinal profile of the magnet prototype (where the Lie2 integration is also applied). The residual $b_{n,B}L_B$ (body part) is computed from the following equation and equally distributed on 16 multipolar kicks, as in the HE method. No random integrated strength is considered in the Heads in this approach.

$$b_{n,B}L_B = b_{n,T}L_T - (b_{n,CS}L_{CS} + b_{n,NC}L_{NC}) \quad (8)$$

$$L_B = L_T - (L_{CS} + L_{NC}) \quad (9)$$

It is worth noticing that the integrated strength in each Head is the same as in the Lie2 model and that the total integrated strength of the magnet is preserved for all the three models, except for the derivatives of the gradient.

4. Amplitude detuning

The Amplitude Detuning corresponds to the variation of the phase-space angular velocity as a function of the Betatron Amplitude. In this paper, we simulate the particles motion over 10^3 revolutions purely on the vertical or horizontal plane, without the dodecapole correction. The initial positions are set to be below the DA value (i.e. $0<2\mathrm{J}_u \leq 0.05\,\mu$m for a normalized emittance

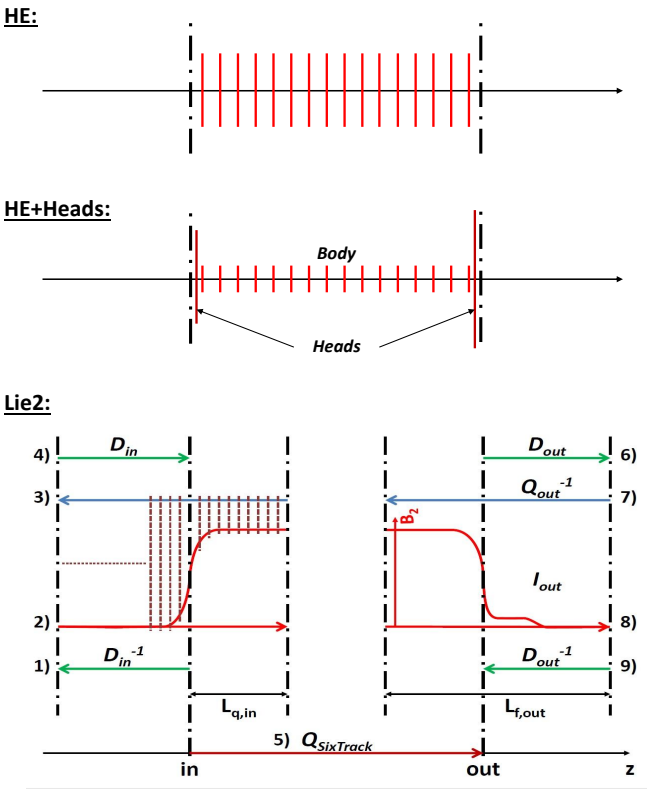

Figure 3: Longitudinal representation of the Models.

of 2.5 μm), and their initial momentum offset δ is 0. As a comparison, the maximum measured amplitude reached in the LHC is of the order of 0.3 μm for a β^* of 25 cm (see Ref. [20, 21, 11]).

For the sake of the graphic visibility, the b_4 multipole error components have been removed from the simulation. And the linear amplitude detuning from the main sextupole second order has been subtracted in the AD using the linear coefficient C1 (about $1.8 \pm 0.1 \times 10^{-2}\,\mu\mathrm{m}^{-1}$ and $1.75 \pm 0.1 \times 10^{-2}\,\mu\mathrm{m}^{-1}$, in the x and y-planes respectively) compatible with the 1^{st} order anharmonicity given by MADX PTC (Ref. [22]).

4.1. Amplitude detuning with all the harmonics

Figure 4 shows the simulated Amplitude Detuning in both planes with all the non-linear errors (except for b_4) for all the models. The horizontal error bars correspond to the minimum and maximum amplitude over the 10^3 revolutions and are centered on the initial amplitude. The vertical error bars correspond to the uncertainty of the correction for linear detuning due to second order effects from main sextupoles. Table 1 shows the fitted values with respect to the predicted ones. For each model, the simulated AD is compared to the theoretical

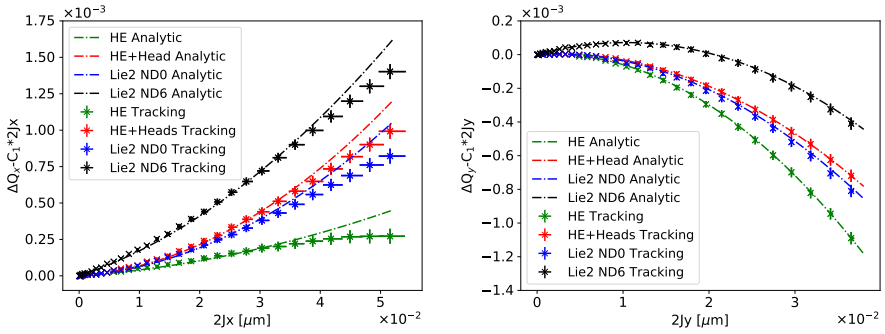

Figure 4: Amplitude detuning for the horizontal (left) and the vertical plane (right).

AD from equations (4) and (5). The simulated detuning with amplitude is fitted with a 4^{th} order polynomial (motivated by using smallest degree for the best score, and its robustness over fitting procedures).

It appears clearly in Fig. 4 and Tab. 1 that the Amplitude Detuning is sensible to the longitudinal distribution of the harmonics in the magnet, i.e. the model. This is also confirmed by the fact that the simulations agree well with the prediction up to an amplitude of $\sim\ 3.0 \times 10^{-2}\,\mu$m.

The good agreement between the HE+Heads and the Lie2 ND0 model shows that one additional kick in each of the extremity gives a good approximation of the longitudinal distribution of the expected non-linearities. Nevertheless, the Lie2 model yields the best representation, if accuracy is more important than computational cost.

The discrepancy between the Lie2 models with and without derivatives (ND0 and ND6, respectively) shows an additional linear detuning generated by the 1^{st} and 2^{nd} derivatives of the b_2 harmonics, as expected from equations (4) and (5). We just note that this effect is of the same order as the effect due to the 2^{nd}-order Sextupoles for the ATS optics [23] with 15 cm β^*, foreseen for HL-LHC project.

Table 1: Amplitude detuning coefficients from Fig. 4 fitted with a 4^{th}-order polynomial and for an Amplitude in μm.

	Analytic		Theory	
Case	$\partial Q_x/\partial(2J_x)$	$\partial^2 Q_x/\partial(2J_x)^2$	$\partial Q_x/\partial(2J_x)$	$\partial^2 Q_x/\partial(2J_x)^2$
HE	$(0.1 \pm 0.3) \times 10^{-3}$	0.08 ± 0.03	0	0.11
HE+Heads	$(0.1 \pm 0.4) \times 10^{-3}$	0.38 ± 0.03	0	0.39
Lie2 ND0	$(0.9 \pm 0.4) \times 10^{-3}$	0.22 ± 0.03	0	0.33
Lie2 ND6	$(9.2 \pm 0.4) \times 10^{-3}$	0.25 ± 0.03	10.9×10^{-3}	0.33
Case	$\partial Q_y/\partial(2J_y)$	$\partial^2 Q_y/\partial(2J_y)^2$	$\partial Q_y/\partial(2J_y)$	$\partial^2 Q_y/\partial(2J_y)^2$
HE	$(0.2 \pm 0.4) \times 10^{-3}$	-0.98 ± 0.05	0	-0.90
HE+Heads	$(0.0 \pm 0.4) \times 10^{-3}$	-0.63 ± 0.05	0	-0.62
Lie2 ND0	$(0.4 \pm 0.5) \times 10^{-3}$	-0.79 ± 0.06	0	-0.67
Lie2 ND6	$(10.7 \pm 0.4) \times 10^{-3}$	-0.67 ± 0.05	10.9×10^{-3}	-0.67

4.2. Amplitude detuning for only the b_6 harmonics

In order to understand the origin of the discrepancy for amplitude higher than $3.0 \times 10^{-2}\,\mu$m in Fig. 4, the same analysis is repeated considering only the b_6 harmonics error in the final focus quadrupoles. Since the error are generated using random number as explained in 3, the second order AD will be different from the previous section. The results are shown in Fig. 5 and Tab. 2.

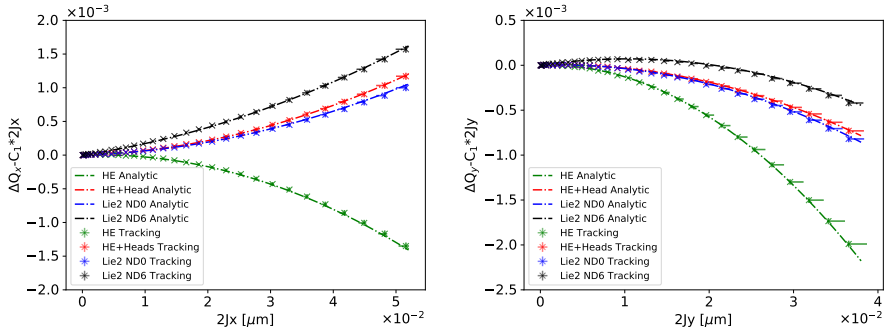

Figure 5: Amplitude detuning for the horizontal plane (left) and the vertical plane (right).

In this case, there is no discrepancy between the theory and the simulation for all the models. This comforts us in the idea that the previous discrepancy comes from higher order harmonics that are not taken into consideration in the analytic calculation.

Table 2: Amplitude detuning coefficients from Fig. 5 fitted with a 4^{th}-order polynomial and for an Amplitude in μm.

	Analytic		Theory	
Case	$\partial Q_x/\partial(2J_x)$	$\partial^2 Q_x/\partial(2J_x)^2$	$\partial Q_x/\partial(2J_x)$	$\partial^2 Q_x/\partial(2J_x)^2$
HE	$(0.8 \pm 0.3) \times 10^{-3}$	-0.64 ± 0.03	0	-0.58
HE+Heads	$(0.6 \pm 0.3) \times 10^{-3}$	0.38 ± 0.03	0	0.39
Lie2 ND0	$(0.7 \pm 0.4) \times 10^{-3}$	0.28 ± 0.03	0	0.33
Lie2 ND6	$(11.4 \pm 0.4) \times 10^{-3}$	0.34 ± 0.04	10.9×10^{-3}	0.33
Case	$\partial Q_y/\partial(2J_y)$	$\partial^2 Q_y/\partial(2J_y)^2$	$\partial Q_y/\partial(2J_y)$	$\partial^2 Q_y/\partial(2J_y)^2$
HE	$(-0.2 \pm 0.5) \times 10^{-3}$	-1.64 ± 0.07	0	-1.59
HE+Heads	$(-0.5 \pm 0.5) \times 10^{-3}$	-0.59 ± 0.06	0	-0.62
Lie2 ND0	$(-0.3 \pm 0.5) \times 10^{-3}$	-0.74 ± 0.07	0	-0.67
Lie2 ND6	$(11.0 \pm 0.4) \times 10^{-3}$	-0.80 ± 0.05	10.9×10^{-3}	-0.67

4.3. Correction of the non-linearities

As mentioned in the previous section, the Detuning with Amplitude and similarly all the RDTs are sensitive to the longitudinal distribution of the high order field harmonics. Since the non-linear corrections are computed in order to cancel the main RDTs, as a result, the correctors strength used to correct them is also sensitive to the longitudinal distribution of the non-linearities.

In HL-LHC, there is one corrector on each side of each IP and their strength is computed using (Ref. [12]):

$$\begin{pmatrix} K_{n,Left}L \\ K_{n,Right}L \end{pmatrix} = \begin{pmatrix} \beta_{x,Left}^{n/2} & \beta_{x,Right}^{n/2} \\ \beta_{y,Left}^{n/2} & \beta_{y,Right}^{n/2} \end{pmatrix}^{-1} \sum_{s \in IP} b_{n,s} K_{r,s} L_s \begin{pmatrix} \beta_{x,s}^{n/2} \\ \beta_{y,s}^{n/2} \end{pmatrix} \quad (10)$$

As the exact values of the strength of each of the magnets errors are not known yet, the strength of the octupole and dodecapole correctors are computed for 60 different seeds, in which the uncertainty and random component of the errors for each magnets can vary according to Eq. 11.

$$b_n = b_{n_S} + \frac{\xi_U}{1.5} b_{n_U} + \xi_R b_{n_R} \quad (11)$$

It represents the sum of a systematic part b_{n_S} and two random parts b_{n_U} and b_{n_R}, normalized with respect to the reference magnet strength [24]. ξ_U and ξ_R denote random variables with Gaussian distribution truncated at 1.5 and 3σ, respectively. In particular, the ξ_U is kept constant for all the inner triplet magnets of the same type (to account for systematic errors coming from different production chains), while ξ_R changes for each magnet (to describe differences between each magnets).

Figure 6 shows the correlation of the non-linear correctors strength at both sides of the high luminosity IPs for these 60 seeds. Since only the systematic component of the error as a longitudinal distribution (while the uncertainty and random component are equally distributed), it results in a systematic shift between the HE model and the others.

The octupole-like generated by b_2' and b_2'' produces a systematic shift in the octupole corrector strength of about 4% with respect to the b_4 corrector specification given in Ref. [12]. In the case of b_6 correction, the systematic shift is around 13%, always with respect to the present corrector specification.

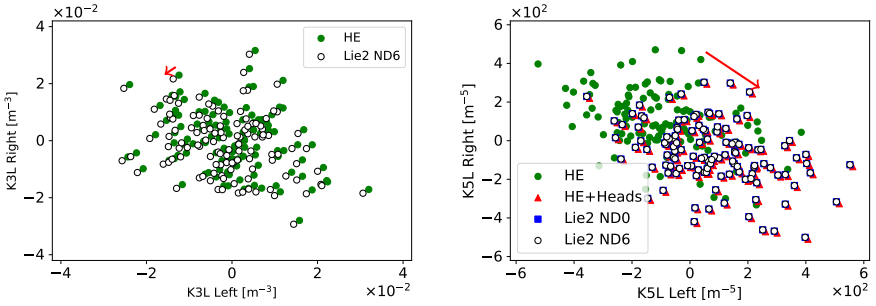

Figure 6: Integrated strength of the b_4 (called KCOX, left) and b_6 (called KCTX right) corrector computed for different models in IR1 and IR5, with 60 seeds.

The shift stays within the correctors specification also for the dodecapole corrector. The difference between the shift for the HE+Heads and the Lie2

models, as well as the effect of the gradients derivatives, is negligible in this case.

It is worth noticing that only the longitudinal distribution of the systematic part of the errors is studied in this paper. The random part of the harmonics is considered equally distributed in the magnet, since this random component is computed using 2D Monte Carlo simulations. Therefore, measurements of the longitudinal profile for all the harmonics (above all the ones that do not have a systematic component) is essential to be able to model them accurately in the calculation of the correction.

5. Dynamic aperture

Dynamic aperture (DA) is a quantity often used to define the performance of an accelerator against magnets imperfections. It is defined as the area of the stable phase-space region spanned by a particle in an accelerator and it is evaluated using particle tracking simulations [25] or measured by different techniques [26].

In this part, we study the impact of the three different models described in section 3 on the computation of DA, focusing in particular on the effect of the b_6 correctors. The DA is computed simulating the particles motion over 10^4 revolutions with initial conditions distributed on a polar grid, so as to have 30 pairs of particles (different initial conditions) for each interval of 2 sigma (beam size) from 0 to 28. Eleven angles in the x-y phase space are scanned, where x and y are in units of linear beam dimensions. The initial momentum offset δ is set to $27.e^{-5}$ (which is equivalent to 2/3 of the LHC RF bucket design). The DA values are defined as the initial amplitudes (in number of beam size σ) of particles lost in 10^4 turns. This procedure for the DA simulations is the same used for LHC DA studies [27] and it was found to provide a precision of about 0.5 beam σ at 10^5 turns [28]. Since in the machine configurations we study in this paper the DA converges very quickly to its asymptotic value, we expect the same type of precision in the DA results of this comparison between models. The tracking simulations in the Lie2 case are performed considering up to two derivatives of the generalised gradient, since there is no significant difference in the tracking with two, four or six number of derivatives of the generalized gradients, see appendix B.

5.1. DA as a function of angles in the x-y phase space

The DA values for the eleven phase space angles scanned in the simulations are shown in Fig. 7 for one configuration of the machine. The cases without and with b_6 correction are compared. DA without b_6 correction is pretty similar for all the model in the x and y plane, while it can differ up to 3 σ at around 40°. The impact of b_6 correction is different according to the model considered. There is no improvement in DA for the HE+heads model while can be significant for the HE or Lie2, according to the angle.

The statistics of all the 60 different configurations of the machine simulated is shown in Fig. 8. Dots represent the values corresponding to the 60 seeds,

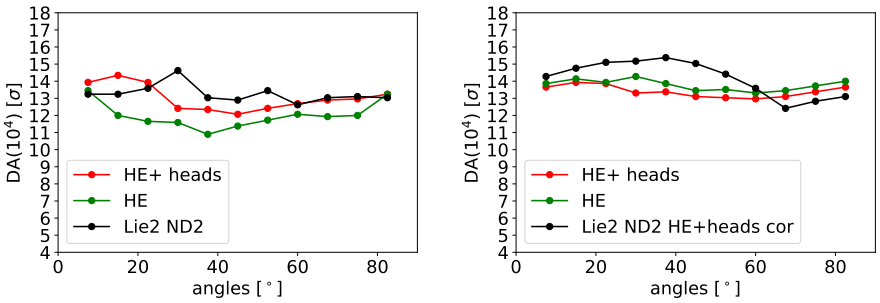

Figure 7: DA at 10^4 as a function of phase space angles with b_6 correctors OFF (left), and with b_6 correctors ON (right) for one configuration of the machine. The HE+Heads model has been used to compute correction of b_6 in the case of Lie2 ND2 tracking.

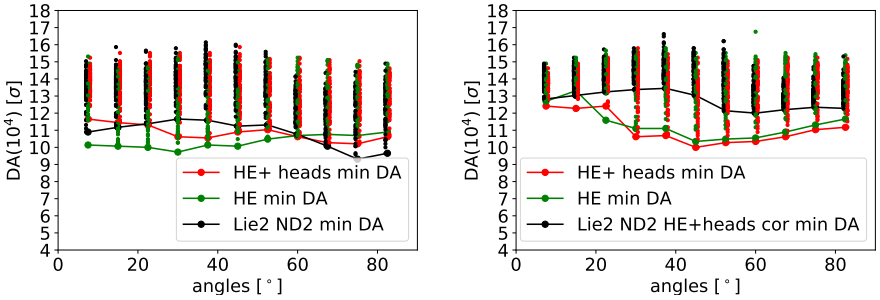

Figure 8: DA at 10^4 as a function of phase space angles with b_6 correctors OFF (left), and with b_6 correctors ON (right). Dots represents the 60 different configurations of the machine according to random component of the magnets errors.

while the continuous line joins the minimum DA values for each angle. All high order fields errors are considered and correction for b_3, b_4, b_5, a_3, a_4, a_5 of the inner triplets, as well as b_3, b_4, b_5 of the arc dipole, are applied. The b_6 correction is included in the results shown in the right panel of Fig. 8. Its effect on DA is slightly different according to the angle and the model. A major positive impact of b_6 correction is visible towards the horizontal plane for the HE model. When the HE+ Heads model is considered the gain in DA is smaller, and in particular the correction does not improve DA for angles around 40°. In the case of the Lie2 model the correction gives a positive impact toward the vertical plane. Averaging over the angles the impact of the b6 correction is of 0σ for the HE+Heads model, 1σ for the HE model and 2σ for the Lie2 model. Finally, a difference between Lie2 model and the two others is visible at 40° when looking at all machine configurations.

5.2. DA as a function of turn

Starting from the ensemble of initial amplitude of particles lost in the x-y phase space, which define the DA shown in the previous section, a normalized

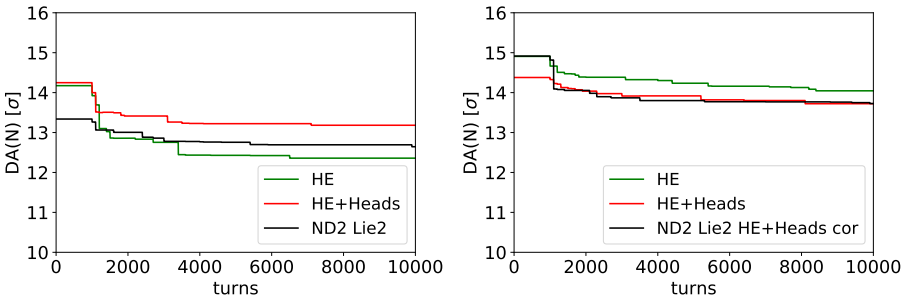

Figure 9: DA as a function of particle revolutions (turns) with b_6 correctors OFF (left), and with b_6 correctors ON (right) for one machine configuration. The HE+Heads model is used to compute the correction in the Lie2 ND2 case.

area of stable motion can be defined following [26]:

$$DA(N) = \frac{2}{\pi} \int_0^{\pi/2} r_s(\theta; N) \mathrm{d}\theta \tag{12}$$

where N is the number of revolutions of the particle in the accelerator (called turns), r_s is the last stable particle (disregarding stability islands non-connected to the origin) and θ is the angle in the x-y phase space. Thus, a value of DA can be calculated for each turn, which is shown in Fig. 9 for one configuration of the machine. In this configuration of the machine (seed), the Lie2 model maintains a higher DA value for longer numbers of turns (above 2000). The impact of the b_6 correction varies according to the model as in the case of the DA vs angle. Once again when the b_6 correction is applied no improvement in the DA evolution is visible for the HE+Heads model.

Figure 10 shows statistics from the 60 different machine configurations. As for the case DA at 10^4 revolutions as a function of the angle, the random part of the errors dominates over the systematic part, resulting in much less difference between the models when looking at their mean values. The only significant difference seems to be on the spread between the minimum and maximum DA values, which is reduced in the Lie2 model, as one can also glimpse in Fig. 8.

6. Conclusion

An analytic expression for Amplitude Detuning and an accurate, symplectic and efficient non linear transfer map are derived, using the generalized gradients representation of the quadrupole vector potential. It allows to quantify the impact of 3D field distribution of the quadrupoles on machine performance, taking into account magnetic field detailed data.

Applied in the case of HL-LHC project, this impact is not negligible and has to be taken into account, especially when comparing computed with beam based measured values. The impact on the b_6 corrector strength can be up to about 13% with respect to the present corrector specification. The impact of the first

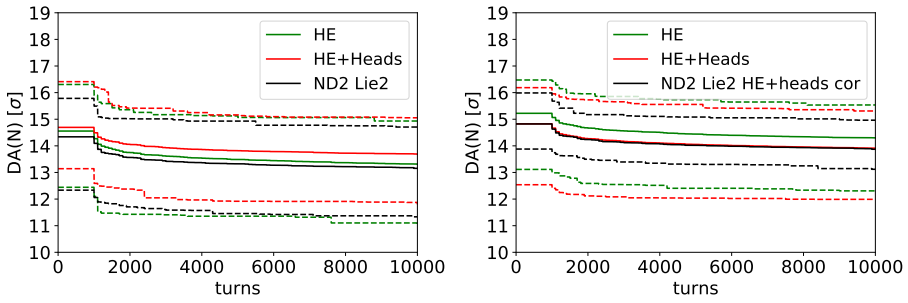

Figure 10: DA as a function of particle revolutions (turns) with b_6 correctors OFF (left), and with b_6 correctors ON (right). The minimum and maximum (dashed lines) together with the mean values (full lines) over 60 different configurations of the machine according to random component of the magnets errors are shown for each model.

and second derivatives of the quadrupole field (octupole-like) accounts for 4% of present octupole corrector specification. The modification to the corrector strength is in the present design specification, so no big impact is expected from the design point of view. Nevertheless, the accurate knowledge of the main field and field errors distribution of the final focus magnets is important to be able to reproduce the long term stability of the machine and the beam based observables in numerical simulations. In particular, being able to reproduce accurately the longitudinal profile of each of the harmonics of the final focus magnets is more important than higher order derivatives. The impact on the computation of dynamic aperture of the b_6 correction can be negligible or amount of about 2σ at 10^4 turns according to the model considered.

This impact, being weighted by the values of the betatronic function at the place where the field errors are located, is expected to be also important in the case of future hadronic circular colliders, such as FCC-hh [29] or more generally when the betatronic function vary a lot inside a magnet.Similarly, the impact of the longitudinal distribution of the field on feed-down effect due to crossing angle or magnet displacement, should also be studied in the future.

7. Acknowledgement

The authors would like to thanks S. Izquierdo-Bermudez and E. Todesco for providing the field harmonics computed with ROXIE of the inner triplet prototype for the HL-LHC project.

Appendices

A. The Lie2 Model and its interface with SixTrack

A.1. The Symplectic map

The Lie2 model developed for this study is derived from the approximated Hamiltonian (Eq. 13) of Ref. [15].

$$K = p_z - a_z - \delta + \frac{(p_x - a_x)^2 + (p_y - a_y)^2}{2(1+\delta)} \tag{13}$$

The vector potential is computed using the Generalised Gradient given by the following equation:

$$C_{n,*}^{[ND]}(z) = \frac{i^{ND}}{2^n n!}\frac{1}{\sqrt{2\pi}}\int_{-\infty}^{+\infty}\frac{k^{n+ND+1}}{I_n'(Rk)}\widehat{B}_{n,*}(R,k)e^{ikz}\mathrm{d}k \tag{14}$$

where the indices s and c correspond to the normal and skew harmonics, respectively. Using this formalism, the normalised vector potential, with respect to the charge q and the total momentum p_0 of the particle, is given by:

$$\begin{aligned}
a_x(x,y,z) &= \frac{q}{p_0 c}\sum_n^\infty\sum_l^\infty\frac{(-1)^l(n-1)!}{2^{2l}l!(l+n)!}\left[\sum_{p=0}^{n/2}\sum_{q=0}^{l}\binom{n}{2p}\binom{l}{q}(-1)^p x^{n+2(l-p-q)+1}y^{2(p+q)}C_{n,s}^{[2l+1]}(z)\right.\\
&\quad\left.-\sum_{p=0}^{(n-1)/2}\sum_{q=0}^{l}\binom{n}{2p+1}\binom{l}{q}(-1)^p x^{n+2(l-p-q)}y^{2(p+q)+1}C_{n,c}^{[2l+1]}(z)\right]\\
a_y(x,y,z) &= \frac{q}{p_0 c}\sum_n^\infty\sum_l^\infty\frac{(-1)^l(n-1)!}{2^{2l}l!(l+n)!}\left[\sum_{p=0}^{n/2}\sum_{q=0}^{l}\binom{n}{2p}\binom{l}{q}(-1)^p x^{n+2(l-p-q)}y^{2(p+q)+1}C_{n,s}^{[2l+1]}(z)\right.\\
&\quad\left.-\sum_{p=0}^{(n-1)/2}\sum_{q=0}^{l}\binom{n}{2p+1}\binom{l}{q}(-1)^p x^{n+2(l-p-q)-1}y^{2(p+q+1)}C_{n,c}^{[2l+1]}(z)\right]\\
a_z(x,y,z) &= \frac{-q}{p_0 c}\sum_n^\infty\sum_l^\infty\frac{(-1)^l(n-1)!(2l+n)}{2^{2l}l!(l+n)!}\left[\sum_{p=0}^{n/2}\sum_{q=0}^{l}\binom{n}{2p}\binom{l}{q}(-1)^p x^{n+2(l-p-q)}y^{2(p+q)+1}C_{n,s}^{[2l]}(z)\right.\\
&\quad\left.-\sum_{p=0}^{(n-1)/2}\sum_{q=0}^{l}\binom{n}{2p+1}\binom{l}{q}(-1)^p x^{n+2(l-p-q)-1}y^{2(p+q)}C_{n,c}^{[2l]}(z)\right]
\end{aligned} \tag{15}$$

Following the technique proposed by H. Yoshida in Ref. [30], a 4D Lie map

(Eq. 16) of second order, that we call Lie2, has been developed.

$$
\begin{aligned}
\begin{pmatrix} p_x \\ p_y \end{pmatrix}_{i+1/7} &= \begin{pmatrix} p_x \\ p_y \end{pmatrix}_{i} + \frac{dz}{2} \begin{pmatrix} \frac{\partial a_z(x_i,y_i,i)}{\partial x} \\ \frac{\partial a_z(x_i,y_i,i)}{\partial y} \end{pmatrix} - \begin{pmatrix} \int \frac{a_x(x_i,y_i,i)}{\partial a_x(x_i,y_i,i)/\partial y} \mathrm{d}x \end{pmatrix} \\
x_{i+2/7} &= x_{i+1/7} + \frac{dz}{2} \frac{p_{x,i+1/7}}{1+\delta} \\
\begin{pmatrix} p_x \\ p_y \end{pmatrix}_{i+3/7} &= \begin{pmatrix} p_x \\ p_y \end{pmatrix}_{i+2/7} + \begin{pmatrix} \int \frac{a_x(x_{i+2/7},y_{i+2/7},i)}{\partial a_x(x_{i+2/7},y_{i+2/7},i)/\partial y} \mathrm{d}x \end{pmatrix} - \begin{pmatrix} \int \frac{\partial a_y(x_{i+2/7},y_{i+2/7},i)}{\partial x} \mathrm{d}y \\ a_y(x_{i+2/7},y_{i+2/7},i) \end{pmatrix} \\
y_{i+4/7} &= y_{i+3/7} + dz \frac{p_{y,i+3/7}}{1+\delta} \\
\begin{pmatrix} p_x \\ p_y \end{pmatrix}_{i+5/7} &= \begin{pmatrix} p_x \\ p_y \end{pmatrix}_{i+4/7} + \begin{pmatrix} \int \frac{\partial a_y(x_{i+4/7},y_{i+4/7},i)}{\partial y} \mathrm{d}x \\ a_y(x_{i+4/7},y_{i+4/7},i) \end{pmatrix} - \begin{pmatrix} \int \frac{a_x(x_{i+4/7},y_{i+4/7},i)}{\partial a_x(x_{i+4/7},y_{i+4/7},i)/\partial y} \mathrm{d}x \end{pmatrix} \\
x_{i+6/7} &= x_{i+5/7} + \frac{dz}{2} \frac{p_{x,i+5/7}}{1+\delta} \\
\begin{pmatrix} p_x \\ p_y \end{pmatrix}_{i+1} &= \begin{pmatrix} p_x \\ p_y \end{pmatrix}_{i+6/7} + \begin{pmatrix} \int \frac{a_x(x_{i+6/7},y_{i+6/7},i)}{\partial a_x(x_{i+6/7},y_{i+6/7},i)/\partial y} \mathrm{d}x \end{pmatrix} + \frac{dz}{2} \begin{pmatrix} \frac{\partial a_z(x_{i+6/7},y_{i+6/7},i)}{\partial x} \\ \frac{\partial a_z(x_{i+6/7},y_{i+6/7},i)}{\partial y} \end{pmatrix}
\end{aligned}
\tag{16}
$$

With this form, the Vector Potential can be computed by slices in z and saved in files, as Horner polynomial coefficients for each step i [19]. These files are then read by the SixTrack code once per simulation Ref. [31, 32].

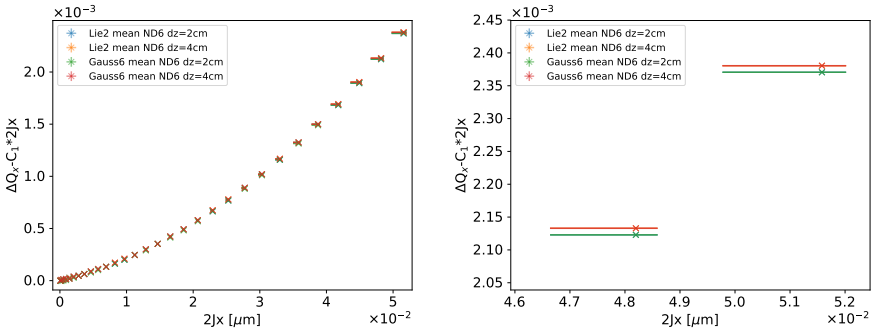

Figure 11: Comparison of the Lie2 model (for ND6) with the referential model (Gauss6) from Ref. [19] on the Amplitude Detuning for two different step sizes in z. The right plot is a zoom over the high amplitude. For each step size, the value for the model are superposed.

In Ref. [19] the accuracy and efficiency of different integration and interpolation methods were studied and compared, including the Lie2 model presented here. In this paper, we compare the tracking using the Lie2 transfer map with the reference model from [19], a 6^{th} order Gauss method, using AD as figure of merit. Figure 11 shows the impact on the AD for the two integration methods and two step sizes. A small difference of about 10^{-5} appears when going at amplitude higher than $0.02\,\mu$m, which is due to the step size in z. The two integration methods reproduce the same detuning with amplitude for a non-linear transfer map of 2 cm step size. In Fig. 12, two interpolation methods (mean and spline) are compared for two step sizes. The mean interpolation method seems

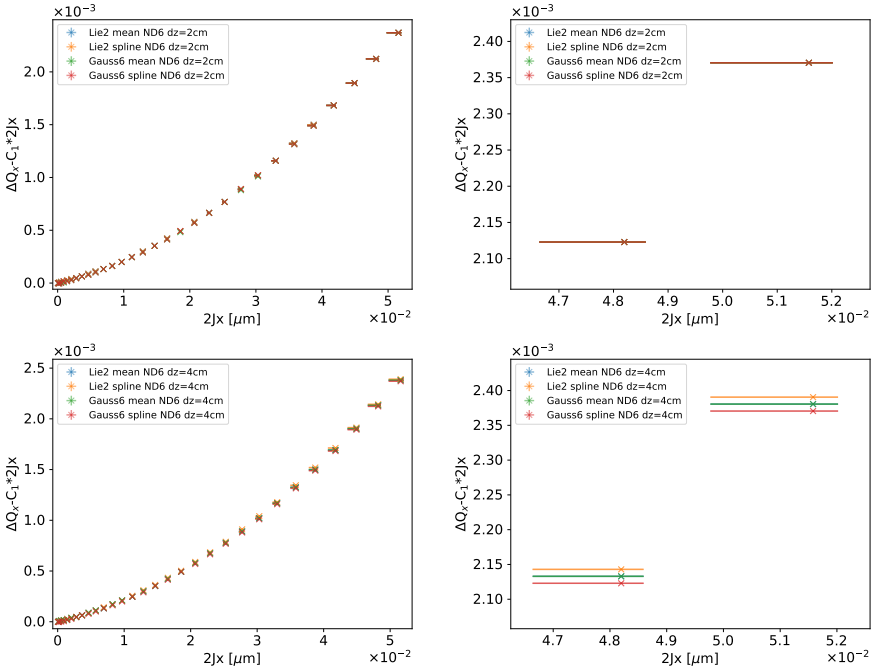

Figure 12: Comparison of the Lie2 model (for ND6) with the referential model (Gauss6) from Ref. [19] on the Amplitude Detuning for dz =2 cm (top) and 4 cm (bottom). The right plot is a zoom over the high amplitude. All the points for dz =2 cm and the mean points for dz =4 cm are superposed.

more stable, with an error of the order of 10^{-5} which is also the precision of frequency analysis. We conclude that the step size in z has more impact on the precision of the model than the integration or the interpolation method chosen, which is also consistent with the results published in Ref. [19].

A.2. The interface of the Lie2 map with Sixtrack

The Head is the region of the magnet in which the harmonics vary along the magnetic axis z. On the contrary the body is the region of constant field (main and higher order harmonics) along z. In other terms the Heads are defined as $\{z \in \mathbb{R} \ : \ B_z(x,y,z) \neq 0, \ \ \forall\ x,y \in \mathbb{R}\}$, i.e. $\{z \in \mathbb{R} \ : \ A_x(x,y,z) \neq 0$ or $A_y(x,y,z) \neq 0, \ \ \forall\ x,y \in \mathbb{R}\}$. With this definition, an equivalent magnetic length is computed for each Head. In Fig. 3, this length is called $L_{q,*}$ (with $*$ being "*in*" and "*out*" for each extremity of the magnet, respectively).

As mentioned previously, the Lie2 model has been implemented in SixTrack (Ref. [32]). In order to add only the non-linear effects of the Fringe Field, and to leave the modelization of the linear part to SixTrack, the first step consists in identifying the beginning of the Hard-Edge quadrupole ("*in*" in Fig. 3). From this position, the particle are tracked back with an anti-Drift of length $L_{D,in} = L_{f,in} - L_{q,in}$, where $L_{f,*}$ is the total length in z of the Vector Potential Files for

the first extremity ((1) in Fig. 3). The forward tracking is then done using the Lie2 map and the Horner coefficient from the first Vector Potential Files ((2) in Fig. 3). At the end of the Lie2 tracking, the linear part has to be removed by using an Half-Kick/Drift/Half-Kick anti quadrupole matrix for each step i ((3) in Fig. 3). The particle is back to the beginning of the Vector Potential File, a Drift of length $L_{D,in}$ returns it to the beginning of the Hard-Edge quadrupole ((4) in Fig. 3). SixTrack takes care of the tracking in the body of the magnet. At the end of the quadrupole, the sequence is reversed (from (6) to (9) in Fig. 3) with the second Vector Potential Files.

As the tracking takes a lot of time (small step size, number of harmonics, number of gradients derivatives, etc), the speed of the routine is a major factor in the choice of the integrator. From [19], two integrators show a low computational time. Since the 4^{th} Runge-Kutta is not symplectic, the Lie2 model is chosen for the SixTrack. A lot of improvements have been made in the optimization of the subroutine. In particular, since storage matrix for the vector potential coefficient (with Horner exponent as coordinate) are relatively sparse, they were saved as a Matrix Market Exchange format (Ref. [33]) also known as COO format (Ref. [34, 35]). This reduces the memory size and increases the speed of Horner polynomial subroutines. Similarly, the power of the horizontal and vertical coordinates are computed beforehand in order to not repeat the same operation during tracking. This allows to multiply the speed of the tracking by a factor of two.

B. The impact of the derivatives

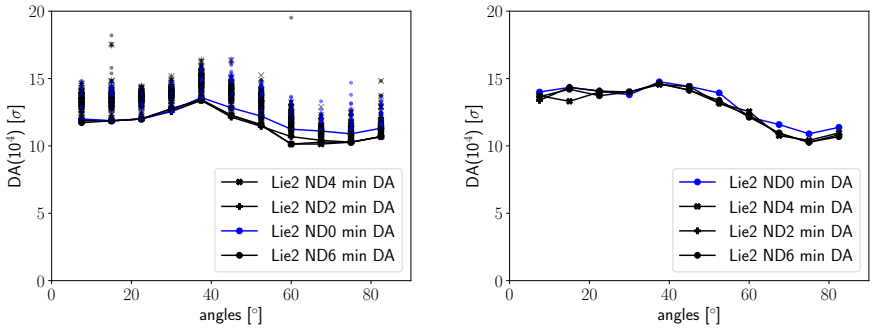

Figure 13: DA as a function of phase space angles (with b_6 correction) for different numbers of gradients derivatives considered in the Lie2 model. All the 60 seeds simulated are shown on the left, while the comparison for one configuration of the machine is shown on the right.

As discussed in section 3, in the case of Lie2 the numbers of gradients derivatives (derivative orders) can be specified in the reconstruction of the vector potential used for the tracking. Figure 13 shows the impact of different number of derivatives on DA. All 60 seeds and the line joining the minimum value for each angle are shown on the left panel, while the comparison for one configuration

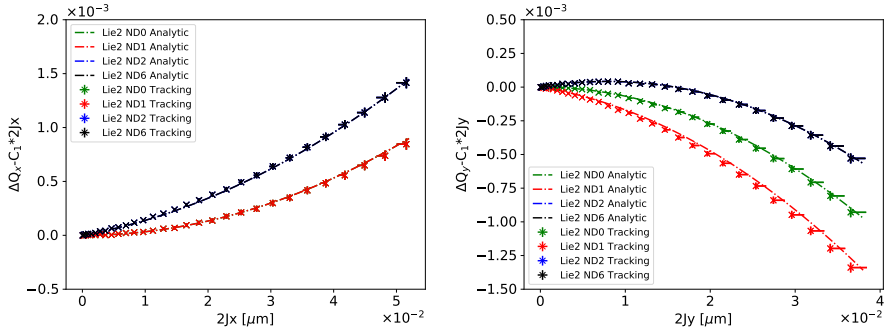

Figure 14: Horizontal (left) and vertical (Right) Amplitude Detuning for different numbers of gradients derivatives considered in the Lie2 model. The Vector Potential is computed with the Horizontal Free Coulomb gauge (see Ref. [19]).

of the machine is shown on the right. All derivatives above the second do not change DA, meaning that only the first two derivatives can be used.

Figure 14 shows a similar comparison for the Amplitude Detuning. It appears that the 1st derivative generates half of the 1st-order Amplitude Detuning. This is not observed for the Horizontal plane because of the Gauge used. In order to further speed-up tracking the horizontal-free Coulomb gauge is chosen, which requires in general between 20% and 25% less coefficients evaluation of the vector potential in Eq. 15 with respect to the azimuthal-free gauge [19]. Nevertheless for even number of derivatives (ND) all the gauges produce exactly the same magnetic field by definition, and as a consequence will result in the same amplitude detuning. It is also important to note that no significant discrepancy can be observed for a number of derivatives (derivative orders) higher than 2, as in the DA case.

References

[1] G. Apollinari, I. Bejar, O. Bruning, P. Fessia, M. Lamont, L. Rossi, T. Tavian, eds., High-luminosity large hadron collider (HL-LHC): Technical design report V. 0.1, Cern yellow report, CERN, Geneva, Switzerland, `https://cds.cern.ch/record/2284929` (2017).

[2] E. Forest, J. Milutinovic, Leading order hard edge fringe fields effects, Nuclear Instruments and methods A 269 (1988) 474–482. `doi:10.1016/0168-9002(88)90123-4`.

[3] Y. Papaphilippou, J. Wei, R. Talman, Deflection in magnet fringe fields, Physical Review E 67 (2003) 046502. `doi:10.1103/PhysRevE.67.046502`.

[4] M. Patecki, R. Tomas, Effects of quadrupole fringe fields in final focus systems for linear colliders, Physical Review Special Topics Accelerators and Beams 17 (2014) 101002. `doi:10.1103/PhysRevSTAB.17.101002`.

[5] B. D. Muratori, J. K. Jones, A. Wolski, Analytical expressions for fringe fields in multipole magnets, Physical Review Special Topics Accelerators and Beams 18 (2015) 064001. doi:10.1103/PhysRevSTAB.18.064001.

[6] M. Venturini, A. J. Dragt, Accurate computation of transfer maps from magnetic field data, Nuclear Instruments and Methods in Physics Research A 427 (1999) 387–392. doi:10.1016/S0168-9002(98)01518-6.

[7] C. E. Mitchell, A. J. Dragt, Accurate transfer maps for realistic beam-line elements: Straight elements, Physical Review Special Topics Accelerators and Beams 13 (2010) 064001. doi:10.1103/PhysRevSTAB.13.064001.

[8] M. Borland, R. R. Lindberg, Modeling of dipole and quadrupole fringe-field effects for the advanced photon source upgrade lattice, in: Proc. of NAPAC, JACoW, Chicago, IL, USA, 2016, pp. 1119–1122, paper THPOA13. doi:10.18429/JACoW-NAPAC2016-TUB2IO01.

[9] A. V. Bogomyagkov, E. B. Levichev, P. A. Piminov, A. Chancé, B. Dalena, J. Payet, R. De Maria, S. Fartoukh, M. Giovannozzi, Analysis of the nonlinear fringe effects of large aperture triplets for the HL-LHC project, in: Proc. 4th International Particle Accelerator Conference, JACoW, Shanghai, China, 2013, pp. 2615–2617, paper WEPEA049.

[10] E. H. Maclean, Modelling and correction of the non-linear transverse dynamics of the LHC from beam-based measurements, Ph.D. thesis, University of Oxford, United Kingdom, CERN-THESIS-2014-135 (2014).

[11] E. H. Maclean, R. Tomás, F. S. Carlier, M. S. Camillocci, J. W. Dilly, J. Coello de Portugal, E. Fol, K. Fuchsberger, A. Garcia-Tabares Valdivieso, M. Giovannozzi, M. Hofer, L. Malina, T. H. B. Persson, P. K. Skowronski, A. Wegscheider, New approach to LHC optics commissioning for the nonlinear era, Physical Review Accelerators and Beams 22 (2019) 061004. doi:10.1103/PhysRevAccelBeams.22.061004.

[12] M. Giovannozzi, S. D. Fartoukh, R. De Maria, Specification of a system of correctors for the triplets and separation dipoles of the LHC upgrades, in: Proc. 4th International Particle Accelerator Conference, JACoW, Shanghai, China, 2013, pp. 2612–2614, paper WEPEA048.

[13] S. White, E. H. Maclean, R. Tomas, Direct amplitude detuning measurement with ac dipole, Physical Review Special Topics Accelerators and Beams 16 (2013) 071002. doi:10.1103/PhysRevSTAB.16.071002.

[14] A. J. Dragt, F. Neri, G. Rangarajan, D. Douglas, L. M. Healy, R. D. Ryne, Lie algebraic treatment of linear and nonlinear beam dynamics, Annual Review of Nuclear and Particle Science 38 (1988) 455. doi:10.1146/annurev.ns.38.120188.002323.

[15] Y. K. Wu, E. Forest, D. S. Robin, Explicit symplectic integrator for s-dependent static magnetic field, Physical Review E 68 (2003) 046502. doi:10.1103/PhysRevE.68.046502.

[16] B. Dalena, O. Gabouev, J. Payet, A. Chancé, R. Brett, R. B. Appleby, R. De Maria, Fringe field modeling for the high luminosity LHC large aperture quadrupole, in: Proc. 5th International Particle Accelerator Conference, JACoW, Dresden, Germany, 2014, pp. 993–996, paper TUPRO002. doi:10.18429/JACoW-IPAC2014-TUPRO002.

[17] T. Pugnat, B. Dalena, A. Simona, L. Bonaventura, R. De Maria, J. Molson, Accurate and efficient tracking in electromagnetic quadrupoles, in: Proc. 9th International Particle Accelerator Conference, JACoW, Vancouver, Canada, 2018, pp. 3207–3210, paper THPAK004. doi:10.18429/JACoW-IPAC2018-THPAK004.

[18] T. Pugnat, B. Dalena, L. Bonaventura, A. Simona, R. De Maria, V. Olsen, Study of fringe fields effects from final focus quadrupoles on beam based measured quantities, in: Proc. 10th International Particle Accelerator Conference, JACoW, Melbourne, Australia, 2019, pp. 90–93, paper MOPGW012. doi:10.18429/JACoW-IPAC2019-MOPGW012.

[19] A. Simona, L. Bonaventura, B. Dalena, T. Pugnat, High order time integrators for the simulation of charged particle motion in magnetic quadrupoles, Computer Physics Communications 239 (2019) 33–52. doi:10.1016/j.cpc.2019.01.018.

[20] E. H. Maclean, F. Carlier, M. S. Camillocci, K. Fuchsberger, M. Giovannozzi, T. H. B. Persson, R. Tomás, Report from LHC MDs 1391 and 1483: Tests of new methods for study of nonlinear errors in the LHC experimental insertions, Report CERN-ACC-NOTE-2018-0035, CERN, Geneva, Switzerland, http://cds.cern.ch/record/2314410 (Jan. 2017).

[21] E. H. Maclean, F. Carlier, J. W. Dilly, M. S. Camillocci, E. Cruz Alaniz, B. Dalena, E. Fol, K. Fuchsberger, M. Giovannozzi, M. Hofer, L. Malina, T. H. B. Persson, J. Coello de Portugal, P. Skowronski, R. Tomás, A. Garcia-Tabares Valdivieso, A. Wegscheider, Report from LHC MD 2158: IR-nonlinear studies, Report CERN-ACC-NOTE-2018-0021, CERN, Geneva, Switzerland, http://cds.cern.ch/record/2306295 (May 2018).

[22] Mad - methodical accelerator design, CERN - BE/ABP Accelerator Beam Physics Group, https://mad.web.cern.ch/mad (may 2019).

[23] S. Fartoukh, Achromatic telescopic squeezing scheme and application to the LHC and its luminosity upgrade, Physical Review Special Topics - Accelerators and Beams 16 (Nov. 2013). doi:10.1103/PhysRevSTAB.16.111002.

[24] S. Fartoukh, O. Brüning, Field quality specification for the LHC main dipole magnets, Report LHC-Project-Report-501, CERN (Oct 2001). URL https://cds.cern.ch/record/522049

[25] E. Todesco, M. Giovannozzi, Dynamic aperture estimates and phase-space distortions in nonlinear betatron motion, Physical Review E 53 (1996) 4067.

[26] E. H. Maclean, M. Giovannozzi, R. B. Appleby, Innovative method to measure the extend of the stable phase-space region of proton synchrotrons, Physical Review Accelerators and Beams 22 (2019) 034002. doi:10.1103/PhysRevAccelBeams.22.034002.

[27] S. Fartoukh, M. Giovannozzi, Dynamic aperture computation for the as-built CERN large hadron collider and impact of main dipoles sorting, Nuclear Instruments and methods A 671 (2012) 10–23. doi:10.1016/j.nima.2011.12.052.

[28] M. Hayes, E. McIntosh, F. Schmidt, The influence of computer errors on dynamic aperture results using SixTrack, LHC Project Note 309, CERN, Geneva, Switzerland, https://cds.cern.ch/record/692073/ (January 2003).

[29] A. Abada, M. Abbrescia, S. S. AbdusSalam, et al., Future circular collider conceptual design report, Report, CERN, Geneva, Switzerland (Jan. 2019). URL https://fcc-cdr.web.cern.ch

[30] H. Yoshida, Construction of higher order symplectic integrators, Physics Letters A 150 (5) (1990) 262 – 268. doi:10.1016/0375-9601(90)90092-3.

[31] SixTrack - 6D tracking code, CERN - BE/ABP Accelerator Beam Physics Group, https://sixtrack.web.cern.ch/SixTrack (jun 2019).

[32] R. De Maria, J. Andersson, V. K. B. Olsen, L. Field, M. Giovannozzi, P. D. Hermes, N. Høimyr, G. Iadarola, S. Kostoglou, E. H. Maclean, E. McIntosh, A. Mereghetti, J. Molson, D. Pellegrini, T. Persson, M. Schwinzerl, B. Dalena, T. Pugnat, I. Zacharov, N. Sjobak, SixTrack version 5: Status and new developments, in: Proc. 10th International Particle Accelerator Conference, JACoW, Melbourne, Australia, 2019, pp. 3200–3203, paper WEPTS043. doi:10.18429/JACoW-IPAC2019-WEPTS043.

[33] Matrix market exchange formats, Matrix Market - NIST, https://math.nist.gov/MatrixMarket/formats.html (aug 2013).

[34] I. P. Stanimirović, M. B. Tasić, Performance comparison of storage formats for sparse matrices, Facta Universitatis (NIŠ). Series Mathematics and Informatics 24 (2009) 39–51.
URL https://facta.junis.ni.ac.rs/mai/mai24/fumi-24_39_51.pdf

[35] R. F. Boisvert, R. Pozo, K. A. Remington, The matrix market exchange format: Initial design, NIST Interagency/Internal Report (NISTIR) 5935 (Dec. 1996).
URL https://citeseerx.ist.psu.edu/viewdoc/download;jsessionid=E98EDA719761E27EFA4969791979893F?doi=10.1.1.34.3448&rep=rep1&type=pdf